

Special Collection

An Easy-to-Use Custom-Built Cell for Neutron Powder Diffraction Studies of Rechargeable Batteries

Daniel Risskov Sørensen,^{*,[a, b]} Andreas Østergaard Drejer,^[c] Michael Heere,^[d, e] Anatoliy Senyshyn,^[f] Matthias Frontzek,^[g] Thomas Hansen,^[h] Christophe Didier,^[i] Vanessa K. Peterson,^[i] Dorthe Bomholdt Ravnsbæk,^[a] and Mads Ry Vogel Jørgensen^[a, b]

In operando powder diffraction remains one of the most powerful tools for non-destructive investigation of battery electrode materials. While in operando X-ray, especially synchrotron radiation, powder diffraction is by now a routine experimental technique, in operando neutron powder diffraction is still less established. We present a new electrochemical cell for in operando neutron powder diffraction, which is, first and foremost, easy to use, but can also cycle electrode materials under electrochemical conditions close to those achieved using

standard laboratory cells. The cell has been designed in multiple sizes, and high-quality electrochemical and neutron powder diffraction data is presented for sample sizes as low as 48 mg total active material. The cell handles lithium-ion and sodium-ion materials equally well, with no difference in how the cell is prepared and assembled. The cell is intended to be used as sample environment at powder diffractometers at the neutron facilities MLZ, ORNL and ACNS.

Introduction

Lithium-ion batteries have been part of every-day life since their commercialization by Sony in 1991. During the entire development period of Li-ion batteries, diffraction techniques have played a central role.^[1,2] Diffraction offers insight into the atomic structure of the electrodes, which in large parts determines the performance of the battery. During the early stages of Li-ion battery research, ex situ X-ray diffraction was most commonly employed by researchers to study electrode materials,^[3–5] but since batteries intrinsically work under non-equilibrium conditions, in situ, or better yet, in operando diffraction experiments are necessary to investigate battery cells under realistic conditions.^[6–8] Structural changes during cycling can be very

different from those deduced from ex situ measurements, and may even depend on the current rate.^[9,10]

Neutron diffraction offers several advantages compared with X-rays:

1. Neutrons have weaker interaction with atoms, leading to a high penetration. This allows for probing the entirety of even thick cells.
2. While the X-ray coherent scattering length is proportional to the electron density resulting in low sensitivity to light elements, the neutron coherent scattering length varies with isotopic composition independently from elemental weights. With a neutron scattering length of -1.9 fm for Li in natural abundance, neutron diffraction is significantly more sensitive

[a] D. Risskov Sørensen, D. Bomholdt Ravnsbæk, M. Ry Vogel Jørgensen
Centre for Integrated Materials Research
Department of Chemistry
University of Aarhus
Langelandsgade 140, 8000 Aarhus C (Denmark)
E-mail: dasoe@chem.au.dk

[b] D. Risskov Sørensen, M. Ry Vogel Jørgensen
MAX IV Laboratory
Lund University
Fotogatan 2, 225 94 Lund (Sweden)

[c] A. Østergaard Drejer
Department of Physics, Chemistry and Pharmacy
University of Southern Denmark
Campusvej 55, 5230 Odense M (Denmark)

[d] M. Heere
Technische Universität Braunschweig
Institute of Internal Combustion Engines
Hermann-Blenk-Straße 42, 38108 Braunschweig (Germany)


[e] M. Heere
Institute for Applied Materials (IAM)
Karlsruhe Institute of Technology (KIT)
Hermann-von-Helmholtz-Platz 1, 76344 Eggenstein-Leopoldshafen (Germany)


[f] A. Senyshyn
Heinz Maier-Leibnitz Zentrum (MLZ)
Technische Universität München
Lichtenbergstr. 1, 85748 Garching b. München (Germany)


[g] M. Frontzek
Neutron Scattering Division
Oak Ridge National Laboratory
1 Bethel Valley Road, Oak Ridge, TN 37831 (USA)

[h] T. Hansen
Institut Laue-Langevin
71 avenue des Martyrs, CS 20156, 38042 Grenoble cedex 9 (France)

[i] C. Didier, V. K. Peterson
Australian Centre for Neutron Scattering
Australian Nuclear Science and Technology Organization
Kirrawee DC, NSW 2232 (Australia)

 Supporting information for this article is available on the WWW under <https://doi.org/10.1002/cmt.202200046>

 Part of a Special Collection on *In Situ and Operando Time-Resolved X-Ray and Neutron Diffraction Studies*. Please visit chemistry-methods.org/collections to view all contributions.

 © 2022 The Authors. Published by Wiley-VCH GmbH. This is an open access article under the terms of the Creative Commons Attribution Non-Commercial NoDerivs License, which permits use and distribution in any medium, provided the original work is properly cited, the use is non-commercial and no modifications or adaptations are made.

than X-ray diffraction to Li in compounds containing heavier elements.

3. Neutron diffraction sometimes offers a better contrast between neighboring elements in the periodic table. This is especially useful for 3d transition metals, where, for example, Mn has a coherent scattering length of -3.73 fm, Co has 2.49 fm and Ni has 10.3 fm. In addition, isotopic substitution can be performed to enhance the contrast between selected elements. This is advantageous as battery cathodes may contain several transition metals.

Several challenges have prevented the full exploitation of the above advantages. The flux at neutron sources is several orders of magnitude lower than at X-ray sources and neutron scattering lengths are also an order of magnitude lower than the corresponding X-ray scattering lengths, which necessitates longer measuring times. Coupled with the lower overall availability of neutrons this leads to a much lower throughput. Hydrogen-containing components like the separator and electrolyte give rise to high incoherent scattering with a large background and a low signal-to-noise as a result.^[11] To overcome this, hydrogen-poor separators can be used as well as deuterated electrolytes, but these are expensive to a degree that can be prohibitive if several milliliters are used per cell.^[11,12] Battery cells designed for in operando neutron powder diffraction (NPD) should therefore aim to minimize the effect of these drawbacks.^[13]

The development of in operando NPD has been approached from different angles by various research groups. To increase the amount of active material in the neutron beam and mimic commercial cells, multiple authors have constructed rolled cylindrical cells.^[14–19] This approach tends to give a good diffraction signal, but the electrochemistry may suffer as cylindrical cells are challenging to construct. Several grams of active material are usually used, which is not a problem when using commercial electrode powders, but for researchers wanting to investigate novel materials, this may be a restrictive requirement. An extra separator is often used around the exterior of the roll to prevent short-circuiting the cell, but the extra hydrogen increases incoherent scattering.

Pouch cells with a prismatic design holding multiple stacked layers are easier to construct in an academic laboratory and valuable NPD results have been obtained using this cell type.^[12,20,21] However, they suffer from some of the same challenges as the rolled cells with large amounts of material required and hydrogen-containing components. In addition, the cell usually presents a large anisotropic scattering and absorption, leading to diffractograms with a significant decrease in intensity at certain angles unless the cell is continuously rotated.^[22]

A cell type based on a single electrode layer has been previously suggested.^[14,23,24] This geometry is most suited for time-of-flight sources, where the detector banks in the forward- and backscattered positions are used to minimize the effects of the cell anisotropy. The detector banks at 90° are usually not used as the neutron absorption is high in this direction.

Lastly, cell types based on a confined electrode design, where the electrode under study is separated from the rest of

the components, have been reported.^[25–27] This is sometimes called a Swagelok-type cell. The cell is designed so that the beam only illuminates the electrode located at one end of the cell. To get a satisfactory diffraction signal in a reasonable amount of time, the electrode must be rather thick, which may hamper the electrochemical performance. The cell has a cylindrical design to optimize its use at instruments with curved, position-sensitive detectors. Since the diffraction signal is rather isotropic, few corrections need to be made as the path length from sample to detector is equal in all directions, although this is only valid if neutron attenuation is low. Since the cell is rather small, if deuterated electrolytes are used to optimize the signal, only small amounts of the expensive electrolyte are needed, which significantly lowers the price of the experiment. The in operando cell proposed in this work is of this Swagelok-type and makes use of the null-scattering material $\text{Ti}_{2.08}\text{Zr}$ (TiZr for short) for the casing and electrode current collectors. The design is inspired by the pioneering work of Bianchini et al.,^[25] where a number of important changes have been made. Most notably, the cell design does not require an insulating layer of Mylar, which reduces incoherent scattering. The diffraction signal is thus optimized in the current design. The design of insulating gaskets is inspired by the Swagelok™ mechanism for an easier, faster and more reproducible assembly of the cell.

Our aim was to construct a measurement cell with the following requirements:

- Capable of cycling the active material for multiple cycles with a voltage profile as close as possible to what is achieved in a standard laboratory cell.
- Prevent components other than the material under investigation from contributing to diffraction patterns.
- Produce enough diffraction intensity for a total electrode mass significantly under one gram and measurement time below 20 minutes for Rietveld refinements.
- Be easy to use for users not experienced with its design. This is to ensure its usefulness as sample environment at the new in operando diffraction beamline, ErwiN,^[28] at MLZ FRMII, Munich, WAND², HFIR, ORNL and instruments at ACNS, Australia.
- Minimize the amount of deuterated electrolyte required.

The cell is thus aimed at research groups wanting to perform in operando NPD on novel materials, where only limited amounts of material may be available, in contrast to commercial materials where kilograms can be bought. It is also designed to be affordable for small research groups who cannot afford to buy more than a few milliliters of deuterated electrolyte.

In the present work, we discuss the design and electrochemical performance of the cell and present data from in operando NPD experiments performed on the D20, Wombat and WAND² instruments, using two battery chemistries: $\text{LiNi}_{0.5}\text{Mn}_{1.5}\text{O}_4$ (LNMO, $Fd\bar{3}m$), a well-characterized high-voltage Li-ion cathode material, and $\text{Na}_{0.7}\text{Fe}_{1/3}\text{Mn}_{2/3}\text{O}_2$ (NaFM, $P6_3/mmc$), a novel layered Na-ion cathode material.^[29] The cell orientation on the instrument, rarely discussed in the literature, was found to notably affect counting statistics and was thus succinctly

optimized. The suitability of data for Rietveld refinements is assessed and strategies to obtain reproducible parameters are discussed.

Experimental Section

Neutron powder diffraction: In situ and in operando NPD experiments were conducted at three facilities. Measurements on LNMO versus Li-metal were conducted at Wombat,^[30] Opal, Australia, in a cell with an inner diameter of 20 mm. Measurements on NaFM versus Na-metal were conducted at D20,^[31] Institute Laue Langevin (ILL), France, in a cell with an inner diameter of 12 mm. Measurements investigating the influence of experiment geometry were conducted at WAND²,^[32] High Flux Isotope Reactor (HFIR), Oak Ridge National Laboratory (ORNL), USA. All three beamlines combine a large neutron flux with a fast curved area detector. At all instruments, the majority of the cell body was shielded using cadmium foil, with only the very bottom of the cell cup being exposed to the neutron beam. The chronological sequence of experiments was Wombat, D20, WAND².

At Wombat, a vertically focusing Ge 115 monochromator was used to select a wavelength of 1.54 Å at a take-off angle of 90°. A TiZr cell with an inner diameter of 20 mm was used with a total cathode mass of 180 mg, consisting of 80 wt% LNMO (Haldor Topsøe), 10 wt% Super P C45 (Energy) and 10 wt% polyvinylidene difluoride (PVDF, HSV900, MTI Corporation). The cathode powder was pressed uniaxially into the TiZr cup with a steel rod using 4300 bar/14 tons. Two borosilicate glass fiber separators (Whatman GF/B) were added and soaked in 600 µL 1 M LiPF₆ in 50:50 v/v deuterated ethylene carbonate (D4 98%, National Deuteration Facility, Australian Nuclear Science and Technology Organization) and 1,2-dimethyl carbonate (D6 98%, Cambridge Isotope Laboratories) in an argon-filled glovebox. A Li-metal foil, 16 mm in diameter, rolled as thin as possible was placed on top, and the cell was closed. The cell flat surface, where the electrode is located, was perpendicular to the plane formed by the incident beam and detector by placing the cell horizontally, with the cell surface oriented almost parallel to the incident beam (See Figure S1 in Supporting Information). The signal was optimized by slightly tilting the cell surface towards the neutron beam, by around 20°. The beam size was 4×20 mm (width×height). Since the beam is hitting the sample surface at an

angle, this geometry can be considered a reflection geometry. We will refer to this as a horizontal, asymmetric reflection geometry (ARG). The moveable, ³He-filled, curved, 2D detector array allows simultaneous detection at 120° in 2θ. During the data collection, the collimator was oscillated around 1 degree in 0.125-degree steps with complete datasets collected every 8 minutes. The cell was charged and discharged at C/10 between 3.5 and 5.0 V. At the end of each charge, a constant voltage of 5.0 V was applied until a current of C/30 was reached.

At D20, a vertically focusing Ge 115 monochromator was used to select a wavelength of 1.54 Å at a take-off angle of 90°. A TiZr cell with an inner diameter of 12 mm was used with a total cathode mass of 60 mg, consisting of 80 wt% NaFM (synthesized as described elsewhere^[29]), 10 wt% C45 and 10 wt% PVDF pressed uniaxially into the cup using 4300 bar/5 tons. Two borosilicate glass fiber separators soaked in 300 µL 1 M NaClO₄ in deuterated propylene carbonate and a thinly rolled Na-metal anode were used. Similar to the measurements at Wombat, the cell flat surface was perpendicular to the plane formed by the incident beam and detector with the flat surface almost parallel to the incident beam and tilted towards it (ARG), but here the tilt angle was 25°. This particular angle was found by using a step scan where the sample table was rotated in the horizontal plane in 1° steps between 15 and 45°. At each angle, a 1-minute exposure scan was taken without moving the detector. The beam was set to 7 mm wide and approximately 20 mm high using a horizontal and circular slit, respectively, see Figure 1b and 1c. No radially oscillating collimator was used during the experiment. For the in operando experiment, the movable position sensitive detector was moved in 61 steps of 0.05° with an exposure time of 20 seconds for each step, yielding a time resolution of approximately 20 minutes per diffractogram. The cell was charged between 2.2 and 4.3 V at C/20 and discharged at C/40 with respect to the insertion/extraction of one Na-ion per formula unit. At the end of charge, a constant voltage of 4.3 V was applied until a current of C/30 was reached. Previous electrochemical measurements showed that each charge and discharge last for approximately 10 h within the given voltage range using these current rates.

At WAND², a vertically focusing Ge 113 monochromator was used to select a wavelength of 1.486 Å at a take-off angle of 51.5°. A series of measurements were performed on 160 mg and 300 mg of LNMO powders in a 12 mm and 20 mm TiZr cell, respectively. The

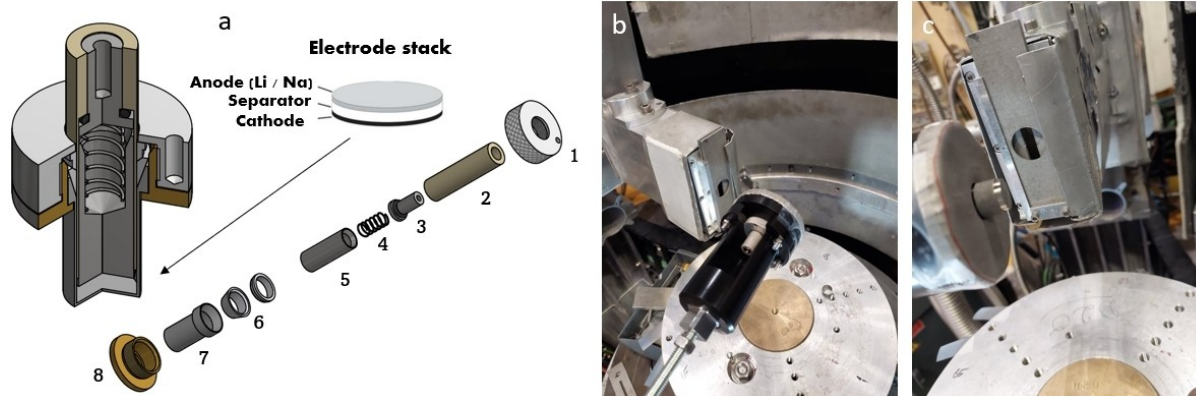


Figure 1. a) Sketch of the 12 mm in operando cell in assembled and exploded view. 1: Upper screw ring. 2: PEEK sleeve. 3: contact pin and O-ring. 4: spring. 5: TiZr anode rod. 6: Teflon gaskets. 7: TiZr cup. 8: Lower screw ring. b) Photograph of the 12 mm cell in the cell holder at D20, ILL, mounted in the horizontal position. The leads are not connected to the cell in the photograph. The incident beam tube is visible to the left and the curved detector array is in the background. c) Photograph of the same setup as in b) from another angle. Note that the bottom part of the cell and cell holder has been covered with cadmium foil. Only the part with the cathode pellet remains exposed to the neutron beam. In front of the beam tube, a 20 mm hole slit, and a 7 mm horizontal slit can be seen.

assembled cell was first mounted vertically in the neutron beam with the cell flat surface in the plane formed by the incident beam and detector with cadmium foil covering all but the bottom 1 mm of the cell cup, and a pattern was collected for 5 minutes. We will refer to this as a vertical transmission geometry (TG). The cell was then mounted horizontally with the cell flat surface perpendicular to the plane formed by the incident beam and detector and the surface of the sample pellets pointing towards the detector (ARG), similarly to the mounting at Wombat and D20. Using the goniometer stage, the cell was rotated in steps of 5 degrees between 0 and 25 degrees. A 5-minute pattern was collected at each angle. The slits were scanned at each geometry to get optimal signal and minimum air scattering.

Rietveld refinement: Sequential Rietveld refinement using the Wombat LNMO data was performed in the TOPAS v6 software.^[33] The crystal structure of $\text{LiNi}_{0.5}\text{Mn}_{1.5}\text{O}_4$ with space group $Fd\bar{3}m$ (ICSD collection code 94762) was used as a starting point for the refinements.^[34] In an attempt to account for what is essentially a thin, flat plate sample in asymmetric reflection geometry (ARG), refinements were performed where sample displacement and intensity correction functions were applied as described by Rowles et al. (thin, flat plate, asymmetric reflection correction model, TFPARC).^[35] The functions are available in the TOPAS software as macros. The pellet thickness used in the macros was 0.2 mm. This number is an average of several measurements on pellets prepared by the procedure described above. The linear attenuation coefficient of LNMO was estimated using a NIST calculator to be 1.174 cm^{-1} .^[36] The tilt angle, ω , with respect to the incoming beam was set to 20° . LNMO has two two-phase transformations during charge and discharge, with especially the first being subtle in terms of shifts in Bragg peaks.^[37] Due to peak overlap, it was not possible to extract precise cell parameters and Li occupancies simultaneously, and we thus opted for two sequential Rietveld refinements using two different strategies. In the first refinement, three distinct phases were included in the structural model, where the Li-occupancy was kept fixed at 1, 0.5 and 0 for the first, second and third phase, respectively. This allowed for the extraction of the cell parameters of the three phases sequentially. For the second refinement, a single phase was used, where the phase transitions were described using a pseudo crystallite size peak broadening model. This allowed for the sequential refinement of the Li-occupancy and oxygen atomic position. For both refinements, the background was described using a 15 coefficient Chebyshev polynomial, and the peak shape was described using a modified Thompson-Cox-Hastings pseudo-Voigt profile. An overall isotropic displacement parameter applied to all atoms and U, V, W profile parameters were refined for the first diffractogram and then kept fixed during the sequential refinements.

Sequential Rietveld refinement of NaFM was conducted using the TOPAS v6 software.^[33] The crystal structure of $\text{P2-Na}_{0.7}\text{Mn}_{0.65}\text{Co}_{0.18}\text{Ni}_{0.17}\text{O}_2$ with space group $P6_3/mmc$ (ICSD collection code 291156) was used as a starting point for the refinements.^[29] As for the Wombat data, an ARG correction was used for sample displacement and peak intensity. The background was described using linear interpolation between manually selected points and peak broadening was modelled with a modified Thompson-Cox-Hastings pseudo-Voigt profile. An overall isotropic displacement parameter applied to all atoms and U, V, W and Y profile parameters were refined for the first diffractogram and then kept fixed during the sequential refinement, where the Na occupancy of the two Na-sites, cell parameters and scale factor were allowed to vary. NaFM disorders at higher voltage, and in patterns where almost no peak intensity is observed, refinements were skipped. In the patterns just before the disorder transition, the Na occupancy was kept constant at previously refined values; the same constraint

was applied for the patterns immediately after the recrystallization on discharge.

The WAND² patterns for LNMO powder were refined with the Rietveld method using the TOPAS v6 software.^[33] A 15 coefficients Chebyshev polynomial was used to describe the background. A scale factor, an overall isotropic displacement parameter applied to all atoms, the lattice parameter, the Li-occupancy, the oxygen atomic position and U, V, W and Y profile parameters were refined for all patterns. In the horizontal ARG, refinements were made with sample displacement and peak intensity corrections, similarly to the Wombat and D20 refinements (no zero-error correction). Refinements were also made where these corrections were not included, and only a zero error correction was included. For the vertical TG, these corrections were not used, and instead, an absorption correction as formulated by Sabine et al. for Debye-Scherrer geometries were used in addition to a zero-error correction.^[38]

Results and Discussion

The in operando cell is described in terms of design, electrochemical performance, experimental setup, and diffraction capabilities. References to the beamtimes at Wombat, D20 and WAND² are made throughout. Subsequently, the results of the in operando NPD experiments and Rietveld refinements are described.

Cell design

To reduce the influence of geometrical effects, a cylindrical cup design was used. The cylindrical design has the added advantage that the electrode powder can be pressed directly into the cup, which is simple and reduces the amount of binder material needed. A sketch of the cell is shown in Figure 1 along with a photograph of the cell in a holder mounted at D20, ILL.

An important aspect of the cell design is its ease of use, which should be intuitive for neutron instrument users who are not familiar with the cell itself, but who have experience assembling lab-scale battery cells like coin cells and Swagelok cells. For the beamtime at Wombat, the measurement was conducted by the beamline staff, who were able to assemble the cell and carry out the experiment with only a short video instruction. The cathode is placed at the bottom of the TiZr cup, and this is the only part of the cell that is exposed to the neutron beam, as the rest is covered in cadmium metal foil. Separator, electrolyte and anode metal foil are then added. Contact is made to the anode metal foil using a TiZr anode rod in the center of the cell. The anode rod is insulated from the cup by a polyether ether ketone (PEEK) sleeve and electrical connection to the anode is made through a spring and a connector pin at the other end of the PEEK sleeve. The connector pin also has an O-ring to make the connection airtight. The spring ensures a constant pressure on the electrode stack. Teflon gaskets around the PEEK sleeve ensure an airtight seal to the TiZr cup. When assembling the cell, the anode is pushed into the cup, loading the spring. When the screw rings are tightened, the Teflon gaskets push inwards on

the PEEK sleeve, preventing it from being pushed out. An important feature of the design is that the center anode rod is only spatially isolated from the cup near the anode foil, that is, no insulating foil is present to prevent short-circuit of the cell like it is seen for other custom-made neutron cells.^[17,19,25] It is a deliberate choice to avoid having such an insulating foil contribute to the scattering signal. While care must be taken when assembling the cell, we have not experienced short-circuits at any point during construction of close to two hundred battery stacks in the cell.

The cell has so far been constructed with three different cup sizes with inner diameters of 8, 12 and 20 mm, respectively. This offers flexibility depending on the specific experiment. Small cells may give better angular resolution and may also be a better choice due to limited availability of cathode powder. Large cells offer more material in the beam for a stronger signal. However, attenuation should also be considered as discussed below. Using custom-made cells with pellets instead of slurry on foils compromises electrochemical performance to achieve a quality diffraction signal. For optimal electrochemical performance, a thin pellet is preferred, while a thick pellet gives a stronger diffraction signal. Empirically, we have found that 0.5 mg cathode powder per mm² gives a good compromise for LNMO or NaFM mixed with 10 wt.% carbon additive and 10 wt.% binder. This corresponds to approximately 25, 57 and 157 mg cathode powder for the 8, 12, and 20 mm cell, respectively. The mass loadings give pellet thicknesses around 0.2 mm for the cathode materials we have investigated so far. It should be noted that using less dense electrode materials would give thicker pellets with these mass loadings, so adjustments may need to be made. The easiest electrode preparation is simply to press the electrode powder into the cup using a uniaxial press. Again empirically, we have used a pressure of around 4300 bar as a suitable rule of thumb, giving 2, 5 and 14 tons for the three cell diameters, respectively. These numbers should be seen only as a guide. In operando diffraction data on the 12 and 20 mm cells only are presented

in this work due to scarcity of beamtime, and the 8 mm cell is not discussed further. The design drawings for the 12 and 20 mm cells are available as Supporting Information.

Electrochemical performance

It is important that the electrochemical response in the in operando cell resembles that of a standard laboratory cell, such as coin and Swagelok type cells. Figure 2a shows a comparison between coated LNMO versus Li-metal in a laboratory Swagelok cell (~3 mg total cathode mass) and LNMO pellets versus Li-metal in a 12 mm and a 20 mm in operando cell (~57 and 154 mg total cathode mass, respectively).

As expected, there is a trade-off in terms of a larger overpotential when using pellets instead of coatings due to the larger thickness of the pellets. The increase in overpotential is in the range of 10–50 mV. Still, similar voltage features and electrochemical response are obtained, and comparable capacities are achieved, suggesting that the electrochemical signal of the in operando cells is representative of what is achieved using coated electrodes. Users may also be interested in cycling electrodes for several cycles either before or during the beamtime, so to probe the long-term cycling capabilities of the cell, a 20 mm cell was cycled at C/5 for 50 cycles, see Figure 2b. After 50 cycles, the capacity had decreased to approximately 90%, which confirms that the cell is indeed able to cycle electrode materials for tens of cycles with a decent capacity retention.

Experimental geometry

As mentioned above, the orientation of the cell with regards to the incident neutron beam is rarely discussed in the literature. On neutron instruments, cylindrical samples are typically measured in transmission geometry (TG), with the cell “bottom”

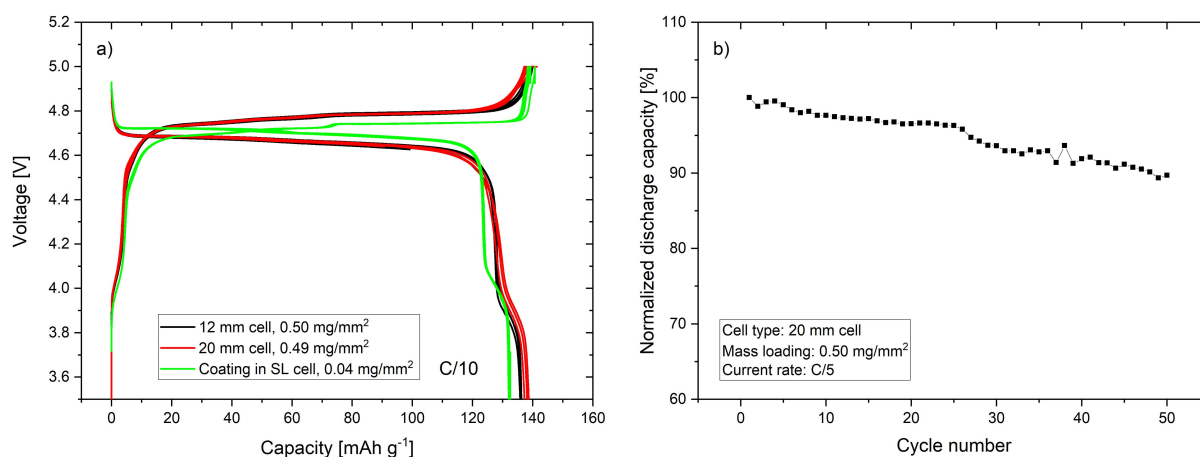


Figure 2. a) Comparison of the electrochemical signal measured on an LNMO coating on aluminum foil in a standard laboratory Swagelok-type cell and pellets in a 12 mm and 20 mm in operando cell. The mass loading in the legend corresponds to the cathode mixture for each cell, where the mass loading of the active material (LNMO) constitutes 80 wt% and the conductive carbon and binder are each 10 wt%. b) Long-term cycling of a 20 mm cell using the same electrode preparation as in a), but the current rate was C/5.

face parallel to the plane formed by the incident beam and the detector. When mounted this way, geometrical effects are minimized as the beam path through the sample is constant at all diffraction angles. However high attenuation can affect peak intensities in a way that is not easily corrected. Bragg reflection intensity increases when the thickness of the cell in the beam is decreased, suggesting relatively strong attenuation from battery materials, perhaps from the presence of Li and H.^[11] By mounting the cell horizontally with the cell flat surface perpendicular to the plane formed by the incident beam and detector, that is, with the surface of the sample pellet pointing towards the detector and tilting it with respect to the neutron beam, Bragg reflection intensity is increased (Figure S1 in Supporting Information). The geometry changes to what can be described as a parallel beam, thin flat-plate asymmetric reflection geometry (ARG), and it can be shown analytically that this increases the intensity for the intermediate angular area compared to TG.^[35] It should be noted that this geometry influences the relative intensities of the Bragg reflections, as the neutrons scattered at angles lower than the tilt angle will pass through more material and thus be absorbed to a higher degree than neutrons scattered at a higher angle. The neutron path through the sample is also not equal at all angles, and corrections are thus necessary for the Rietveld refinement. The effect of the mounting geometry was investigated at WAND², where powders of pure LNMO were pressed into the TiZr cups. The cell was then mounted, first vertically (TG), and then horizontally (ARG) at tilt angles ω between the incident beam and the cell surface from 0 to 25°. The resulting diffractograms are shown in Figure S2. The diffractograms overall show the same Bragg reflections, but the background and peak intensity varies significantly at low 2θ angles. In particular, the LNMO 111 reflection at approximately 18° 2θ loses intensity when ω increases and disappears completely at $\omega=25^\circ$. The background at low 2θ angles is sloping, which increases for increasing ω angles as expected. For the TG cell, the background has a positive slope when moving to lower 2θ angles due to air scattering. The patterns are also slightly noisier and the diffraction peaks less distinct (e.g., 18 and 36° 2θ reflections in Figure S2) compared with the ARG mounting. This is likely due to a significant reduction of the total neutron flux hitting the sample as the beam size is reduced to match the smaller exposed area and attenuation playing a larger role for the TG. In addition, more of the scattered signal is likely absorbed by the cadmium foil. Removing the cadmium foil would likely give a stronger signal for the vertical mounting but would also increase parasitic scattering from other cell components.

To correct for angle dependent geometric aberration effects in the ARG, a thin flat-plate asymmetric reflection geometry model (TFPARG) can be used when performing the Rietveld refinement by using an intensity and sample displacement correction as described by Rowles et al. (Equation 5 and 19, respectively, in the referenced publication)^[35]. An intensity correction factor based on the ratio in diffraction volume between an ARG and a symmetric reflection geometry (SGR, Bragg-Brentano) is given in Equation (1):

$$\frac{V_{ARG}}{V_{SGR}} = I_{scale}^{ARG} = 2 \left(1 + \frac{\sin(\omega)}{\sin(2\theta - \omega)} \right)^{-1} \left(1 - \exp \left(-\mu t \left(\frac{1}{\sin(\omega)} + \frac{1}{\sin(2\theta - \omega)} \right) \right) \right) \quad (1)$$

where ω is the angle between the parallel beam and the sample surface, μ is the linear attenuation coefficient of the sample and t is the thickness. The internal correction routine for Bragg-Brentano geometry within the Rietveld refinement software is then able to read measured intensities correctly by scaling the Bragg peaks by this factor in addition to how the peaks are scaled by the Lorentz factor. A comparison of the refinement results obtained with and without such a correction is shown in Figure S3 along with an example of the intensity correction factor as a function of diffraction angle for $\omega = 20^\circ$. Without correction, the refined oxygen position and Li occupancy depend on ω , with unrealistic values for the occupancy before cycling, confirming the need for an intensity correction. Application of the intensity correction model results in refined values similar to the TG measurements. For the TG measurements, an intensity correction was also performed, but assuming a Debye-Scherrer geometry instead as described by Sabine et al.^[38]

At D20 and Wombat, the cell was mounted horizontally (ARG) and tilted at an angle of about 20–25° with respect to the neutron beam path. At D20, the angle was chosen by performing a stepwise rotation of the sample table (seen in the lower parts of Figure 1b and c) with a 1-minute exposure at each angular step. The resulting intensity plot can be seen in Figure S4 in the Supporting Information. The angle chosen was 25° due to the maximum in peak intensity at this angle. A drawback of the ARG is the risk of a parasitic signal from the metal anode. Due to the high neutron absorption of ⁶Li, only a small Li-metal signal is obtained, but a significant signal can be obtained for Na-metal, as seen below. The neutron absorption by the borosilicate separators is actually an advantage in ARG, as it helps reduce the signal from the metal anode. It should be noted that there seems to be no adverse effects to turning the cell horizontal, as the electrolyte is immobilized in the separators.

In operando NPD on LNMO at Wombat, OPAL

LiNi_{0.5}Mn_{1.5}O₄, LNMO (space group $Fd\bar{3}m$), with Mn and Ni randomly distributed on the transition metal site, was chosen as a model system for the in operando NPD experiment at Wombat (Figure 3). LNMO is a high-voltage, cobalt-free cathode material considered as a candidate for next-generation Li-ion batteries.^[39] For this experiment, the 20 mm TiZr cell was used with a cathode mass of 180 mg, corresponding to 144 mg active material. In the operando NPD data, no reflections are observed for any phase except for the active LNMO material under study. This is a big advantage as reflections from other phases such as copper and aluminum in current collectors can interfere with the Rietveld refinement due to overlap of the

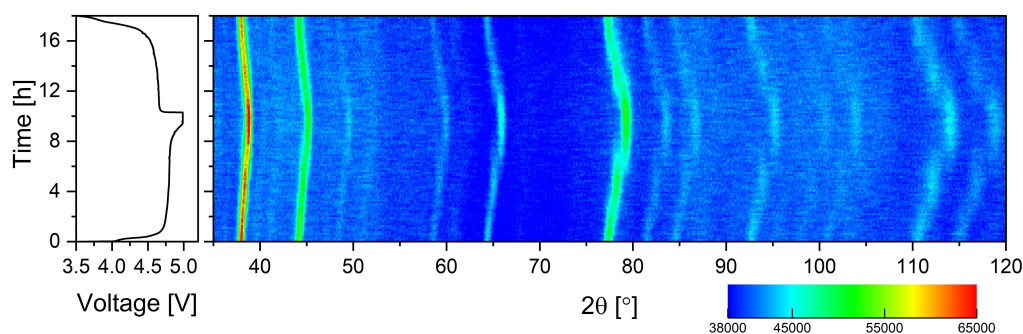


Figure 3. Stack of neutron powder diffraction patterns (intensities in arbitrary units) collected on $\text{LiNi}_{0.5}\text{Mn}_{1.5}\text{O}_4$ versus Li during cell charge/discharge using the 20 mm TiZr cell at C/10. The charge/discharge curves corresponding to the diffractograms are shown in the graph to the left. Measured at Wombat, $\lambda = 1.54 \text{ \AA}$.

reflections. As mentioned above, however, the horizontal mounting can lead to a small Li-metal signal. Expected reflection positions for Li-metal are shown in Figure 4a for comparison, but the phase was not included in the refinement. Small peaks around 51.0 and 87.5° are likely from the Li-anode. The Li-peaks are at 2θ -values slightly below the database reference due to the Li-foil being slightly downstream of the sample thus giving an apparent angular offset. The broad hump at low angles originates from the short-range structure of the deuterated electrolyte.

An overview-plot of the in operando NPD data with stacked diffractograms of the LNMO sample is shown in Figure 3. In some intervals of the charge and discharge (e.g., during the first 2.5 h of charge), a single set of relatively narrow LNMO reflections are observed, which signifies that all the LNMO domains within the electrode have similar Li-contents. In other parts of the charge and discharge (e.g., between 6–8 h) the peaks broaden and even split to two sets of LNMO Bragg reflections. Variation in the peak broadening can be caused by both changing crystallite size and variation in the Li-content

among the LMNO domains, while the observation of the two sets of LNMO reflections signifies that LNMO domains with two distinctly different Li-contents are found in high numbers in the electrode.

To extract quantitative structural information, the 115 operando NPD diffractograms obtained during charge and discharge were analyzed by sequential Rietveld refinement using the structural model for LNMO with the $Fd\bar{3}m$ space group and with Li on the $8a$ site, Mn and Ni on the $16d$ site and O on the $32e$ site.^[34] The first diffractogram used in the sequential Rietveld refinement is shown in Figure 4a along with the resultant fit. Two strategies were used for the sequential Rietveld refinement: In the first, three LNMO phases with fixed Li-content (1.0, 0.5 and 0.0) are used, and the degree of lithiation is obtained through the amount of each phase, that is, the scale factors as well as the unit cell parameters are allowed to vary freely. Unfortunately, due to peak overlap in the regions with two LNMO phases, this strategy does not allow for refinement of Li-occupancies or atomic positions. In the second refinement strategy, a single LNMO phase is used throughout,

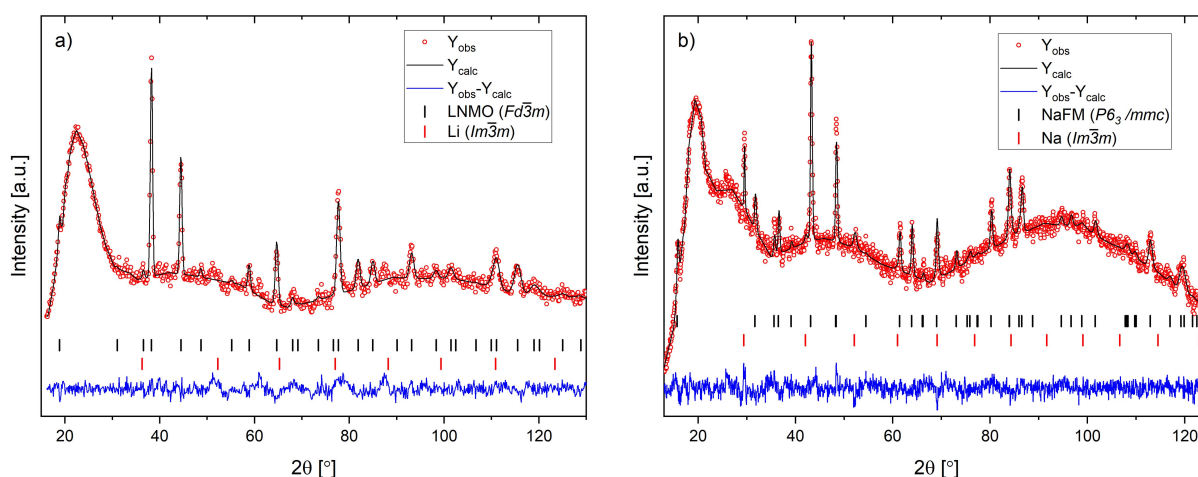


Figure 4. a) First diffractogram during the in operando experiment on LNMO in the 20 mm cell at Wombat. Small Li-metal peaks may be visible around 51.0 and 87.5° , but they were not included in the refinement. They are indicated with asterisks. b) First diffractogram during the in operando experiment on NaFM in the 12 mm cell at D20. Na-peaks can be seen in addition to the NaFM peaks, and a Na-metal phase with the $Im\bar{3}m$ space group was included in the refinement. They are indicated with asterisks.

and the degree of lithiation is refined directly through the Li-occupancy. Additionally, the atomic positions are refined.

Based on the first strategy, the unit cell parameters and the weight percentages of the three observed phases are shown in Figure 5a and 5b as a function of time. This shows that two topotactic two-phase transitions occur on charge and are reversible on discharge with the weight percentages of each phase changing smoothly during the phase transitions as expected. From the second refinement strategy, the unit cell parameter, the pseudo crystallite size (based on the peak broadening model), the Li-occupancy as well as the Li–O and transition metal–O distances are shown in Figure 5c and 5d. This strategy also points to three single-phase regions separated by two-phase transitions through the variations in the crystallite size parameter (Figure 5c), that is, the crystallite size decrease (peaks broaden) during the two-phase transition, while the crystallite size is larger in the single-phase regions wherein the peaks are narrower. As expected, the crystallite size is largest at the beginning and end of charge and discharge, where the end-members exist as a single phase, that is, the Li-content is very homogeneous across all LMNO domains. The refined Li-occupancy decreases steadily throughout the charging process, and increases reversibly during discharge. From the change in the transition metal (TM, Ni or Mn) to oxygen distance, we see a clear shrinkage of the TM-oxygen octahedron during charge.

This is attributed to the oxidation of Ni, which increases the electrostatic attraction between Ni and oxygen. At the same time, the Li-to-O distance also decreases, which reflects the removal of Li from the lattice. On subsequent discharge, these changes revert. Overall, the observed behavior agrees with previous observations of $Fd\bar{3}m$ LNMO during cycling.^[37,40]

In operando NPD on $\text{NaFe}_{1/3}\text{Mn}_{2/3}\text{O}_2$ at D20, ILL

To confirm that the cell is compatible with other battery chemistries than Li-ion, we measured $\text{Na}_{0.7}\text{Fe}_{1/3}\text{Mn}_{2/3}\text{O}_2$ (NaFM) versus Na-metal at D20, ILL, France. NaFM is a layered P2-type cathode material with the $P6_3/mmc$ space group. The structure is shown in Figure S5. NaFM is an interesting material due to its very low cost, as it only contains inexpensive transition metals. The in operando cell is assembled and operated in exactly the same way when using Na-containing anodes and cathodes as when using their Li-containing counterparts. To reduce the incoherent scattering from hydrogen in the electrolyte, NaClO_4 in deuterated propylene carbonate was used. An overview plot of the in operando experiment is shown in Figure 6.

The Bragg peaks from NaFM are clearly visible, but peaks from Na-metal are also present, especially at $\sim 30^\circ 2\theta$, see Figure 4b. Using sequential Rietveld refinement, cell parameters

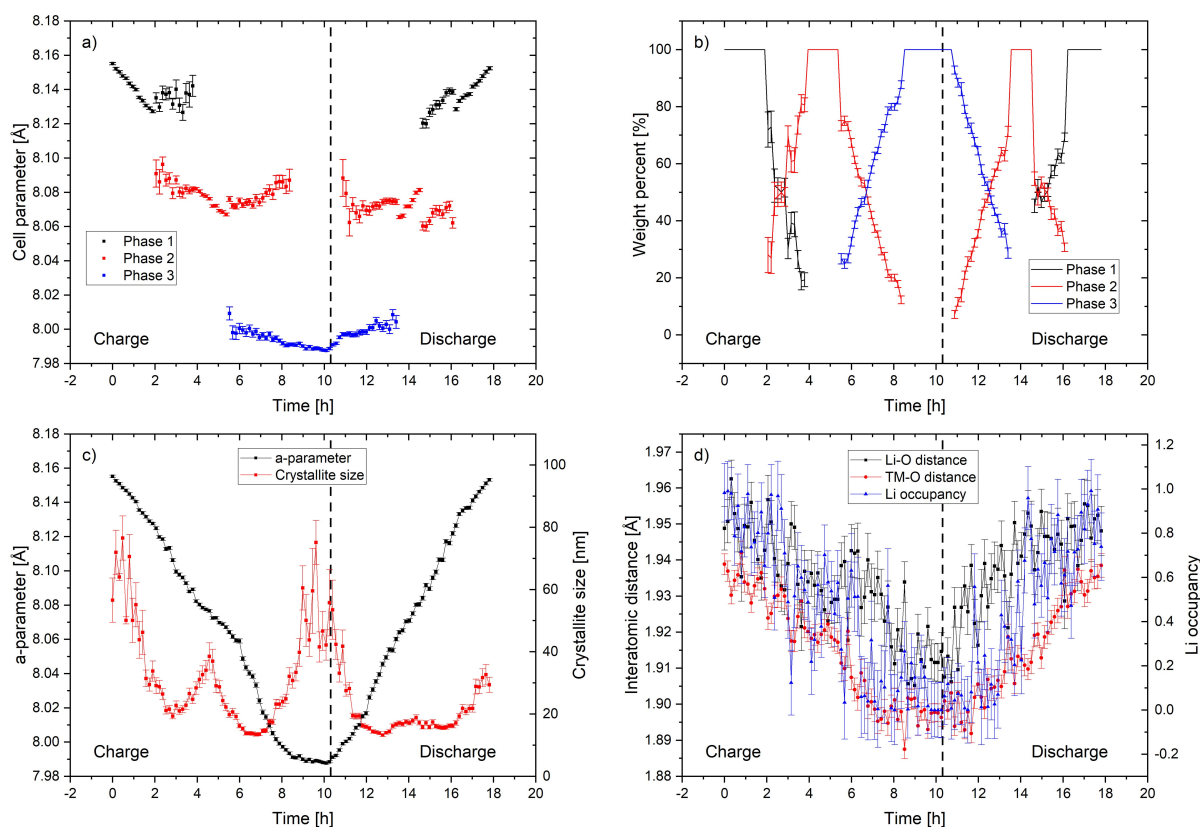


Figure 5. Results of sequential Rietveld refinements as a function of time on LNMO. a) and b) show the results for the multi-phase refinement, while c) and d) show the results from the single-phase refinement. a) Lattice parameter for the three LNMO phases. b) Weight percent for the three LNMO phases. c) Cell parameter and size broadening parameter for the single LNMO phase. d) Interatomic distances and Li occupancy for the single LNMO phase. Error bars represent one estimated standard deviation from individual refinements.

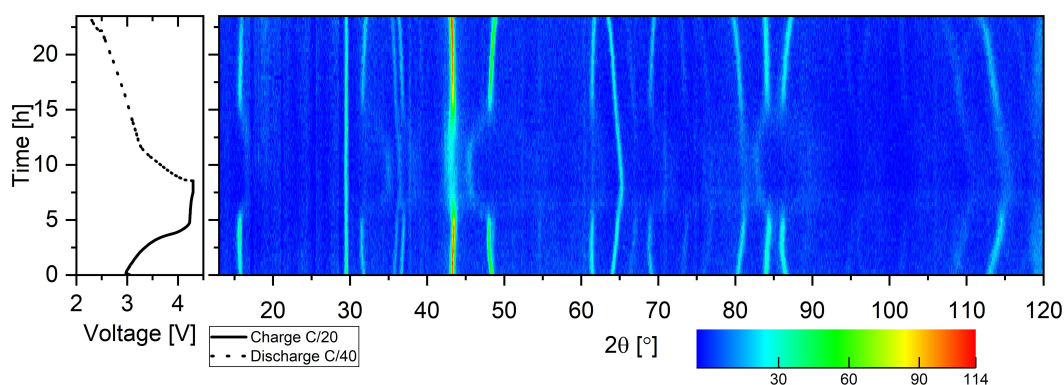


Figure 6. Stack of neutron powder diffraction patterns (intensities in arbitrary units) collected on $\text{NaFe}_{1/3}\text{Mn}_{2/3}\text{O}_2$ versus Na-metal during cell charge/discharge. The charge/discharge curves corresponding to the diffractograms are shown in the graph to the left. The background was subtracted. Measured at D20, ILL, $\lambda = 1.54 \text{ \AA}$.

and Na-occupancies for NaFM could be extracted, see Figure 7. Interestingly, for this material, the material undergoes a reversible order-disorder transition, where almost all Bragg reflections disappear near the end of charge, but reappear

during the subsequent discharge.^[41] Structural details from this part of the experiment can naturally not be elucidated from the NPD data as this will require use of a complementary technique.

The structure evolution is clearly not symmetrical during charge and discharge. This can be gleaned already from the overview plot in Figure 6. During desodiation, the unit cell volume decreases continuously until it reaches a plateau after which the Bragg peaks disappear (Figure 7c). When the Bragg peaks reappear, the volume is significantly larger than the plateau before the disordering and (after a slight decrease) continuously increase during sodiation. Upon further sodiation, the unit cell volume increases to values above the initial volume, indicating that the cathode is sodiated to $x > 0.7$ in $\text{Na}_x\text{Fe}_{1/3}\text{Mn}_{2/3}\text{O}_2$. This is also reflected in unit cell parameters, which evolve to values higher (for the a-axis) and lower (for the c-axis) than the corresponding values at the beginning of the charge. Finally, further insight into the reaction mechanism can be obtained from the Na-site occupancies. During desodiation, Na is extracted primarily from site 2, while the occupancy at site 1 remains rather constant, see the structural model in Figure S5. During resodiation, an equilibration seems to have taken place during the period of low crystallinity as the Na occupancies are now quite similar. The occupancies of both sites increase continuously, but towards the end of the discharge, the site 1 occupancy continues to increase while the site 2 occupancy plateaus. The experiment thus shows that both cell parameters and active ion occupancies can be extracted in operando for an active material mass as low as 48 mg.

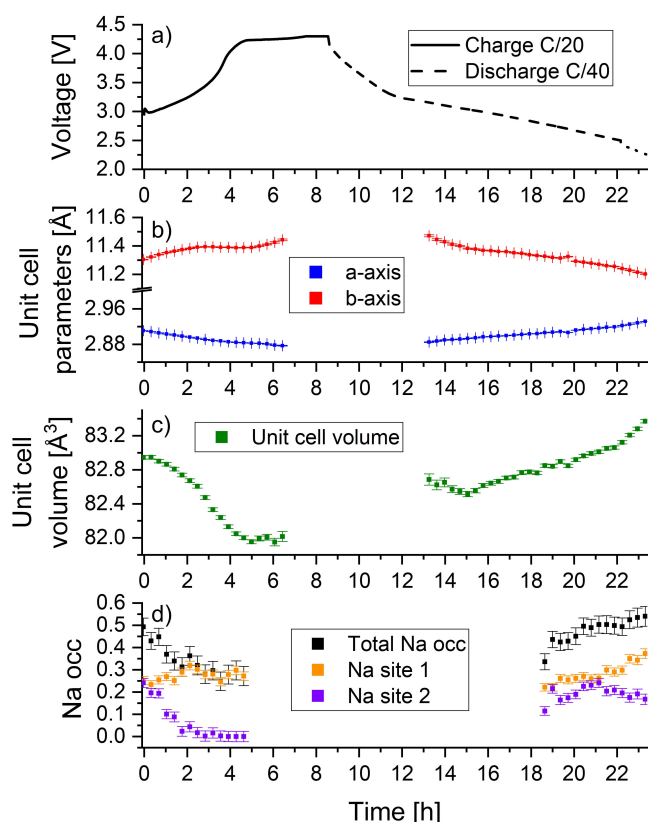


Figure 7. Results for the sequential Rietveld refinement on NaFM. a) Voltage curves for the in operando experiment. b) Unit cell parameters as a function of time. c) Unit cell volume as a function of time. d) Na-occupancies as a function of time. Occupancies for site 1, site 2 and the summed occupancy are shown. The occupancy could not be extracted very close to the disappearance of the Bragg peaks, and they were thus not refined for these diffractograms while the cell parameters were. Error bars represent estimated standard deviations for individual refinements.

Conclusion

An in operando NPD cell was developed based on the Swagelok-type design with an emphasis on ease of use and to maximize the diffraction signal for small sample sizes. Two cell sizes were explored and data sufficient for structural refinement were obtained for selected Li- and a Na- model systems, for an active material mass as low as 48 mg. Electrochemical perform-

ance close to what is achievable in standard lab cell types was presented, which is vital for a cell of this type. The in operando cell can be mounted in a transmission or reflection diffraction geometry and the differences to the diffraction patterns and the Rietveld refinements were explored. Overall, a stronger diffraction signal is obtained in the reflection configuration for the same measurement time, but an attenuation correction is necessary to obtain reliable refinement parameters. For the in operando experiments, both cell parameters and active ion occupancies could be refined, indicating that the cell design is suitable for structural studies on novel materials. We believe that this work moves in operando NPD studies closer to becoming a routine tool in battery science.

Acknowledgements

We would like to thank workshop technician Lars Brændegaard Hansen at the Department of Physics, Chemistry and Pharmacy, University of Southern Denmark. He has played a vital role in both constructing and designing the cell. We also thank Mickey Sejerup Pedersen for supplying $\text{Na}_x\text{Fe}_{1/3}\text{Mn}_{2/3}\text{O}_2$. D.R.S. acknowledges the funding from the project "Operando Neutron Diffraction of Cathode Materials for Rechargeable Li-ion Batteries" with project number 87686 by Nordforsk under the Nordic Council of Ministers. A.Ø.D. and D.B.R. acknowledge the Danish Ministry of Higher Education and Science for funding via the SMART Lighthouse project. M.H. acknowledges the funding from the project 05K16VK2/05K19VK3 "Energy research with Neutrons (ErwiN)" by the German Federal Ministry of Education and Research (BMBF). D.R.S., A.Ø.D. and D.R.B. thank Danscatt for funding travel costs related to the neutron diffraction experiments. We thank ANSTO for beamtime at Wombat (proposal number P8958). We also thank T. Darwish and N. Yepuri from the National Deuteration Facility for synthesizing deuterated ethylene carbonate (proposal number CB8567). We acknowledge the beamtime at D20, ILL (proposal 5-23-740. Data reference: doi:10.5291/ILL-DATA.5-23-740). This research used resources at the High Flux Isotope Reactor and Spallation Neutron Source, DOE Office of Science User Facilities operated by the Oak Ridge National Laboratory.

Conflict of Interest

The authors declare no conflict of interest.

Data Availability Statement

The data that support the findings of this study are available from the corresponding author upon reasonable request.

Keywords: in operando · Li-ion battery · materials science · Na-ion battery · neutron diffraction

- [1] K. Mizushima, P. C. Jones, P. J. Wiseman, J. B. Goodenough, *Mater. Res. Bull.* **1980**, *15*, 783–789.
- [2] J. N. Reimers, J. R. Dahn, *J. Electrochem. Soc.* **1992**, *139*, 2091–2097.
- [3] M. M. Thackeray, *Prog. Solid State Chem.* **1997**, *25*, 1–71.
- [4] A. K. Padhi, K. S. Nanjundaswamy, C. Masquelier, J. B. Goodenough, *J. Electrochem. Soc.* **2019**, *144*, 2581–2586.
- [5] N. Yabuuchi, T. Ohzuku, *J. Power Sources* **2003**, *119–121*, 171–174.
- [6] A. V. Llewellyn, A. Matruglio, D. J. L. Brett, R. Jervis, P. R. Shearing, *Condens. Matter* **2020**, *5*, 75.
- [7] S.-M. Bak, Z. Shadike, R. Lin, X. Yu, X.-Q. Yang, *NPG Asia Mater.* **2018**, *10*, 563–580.
- [8] D. Liu, Z. Shadike, R. Lin, K. Qian, H. Li, K. Li, S. Wang, Q. Yu, M. Liu, S. Ganapathy, X. Qin, Q. H. Yang, M. Wagemaker, F. Kang, X. Q. Yang, B. Li, *Adv. Mater.* **2019**, *31*, e1806620.
- [9] D. B. Ravnsbaek, K. Xiang, W. Xing, O. J. Borkiewicz, K. M. Wiaderek, P. Gionet, K. W. Chapman, P. J. Chupas, Y. M. Chiang, *Nano Lett.* **2014**, *14*, 1484–1491.
- [10] H. Liu, F. C. Strobridge, O. J. Borkiewicz, K. M. Wiaderek, K. W. Chapman, P. J. Chupas, C. P. Grey, *Science* **2014**, *344*, 1252817.
- [11] G. Liang, C. Didier, Z. Guo, W. K. Pang, V. K. Peterson, *Adv. Mater.* **2020**, *32*, e1904528.
- [12] W. K. Pang, V. K. Peterson, *J. Appl. Crystallogr.* **2015**, *48*, 280–290.
- [13] N. Sharma, W. K. Pang, Z. Guo, V. K. Peterson, *ChemSusChem* **2015**, *8*, 2826–2853.
- [14] J. J. Biendicho, M. Roberts, C. Offer, D. Noréus, E. Widenkvist, R. I. Smith, G. Svensson, K. Edström, S. T. Norberg, S. G. Eriksson, S. Hull, *J. Power Sources* **2014**, *248*, 900–904.
- [15] W. R. Brant, S. Schmid, G. Du, H. E. Brand, W. K. Pang, V. K. Peterson, Z. Guo, N. Sharma, *J. Visualized Exp.* **2014**, *93*, e52284.
- [16] L. Boulet-Roblin, P. Borel, D. Sheptyakov, C. Tessier, P. Novák, C. Villevieille, *J. Phys. Chem. C* **2016**, *120*, 17268–17273.
- [17] W. R. Brant, M. Roberts, T. Gustafsson, J. J. Biendicho, S. Hull, H. Ehrenberg, K. Edström, S. Schmid, *J. Power Sources* **2016**, *336*, 279–285.
- [18] L. Boulet-Roblin, D. Sheptyakov, P. Borel, C. Tessier, P. Novák, C. Villevieille, *J. Mater. Chem. A* **2017**, *5*, 25574–25582.
- [19] N. Sharma, G. Du, A. J. Studer, Z. Guo, V. K. Peterson, *Solid State Ionics* **2011**, *199–200*, 37–43.
- [20] C. J. Chen, W. K. Pang, T. Mori, V. K. Peterson, N. Sharma, P. H. Lee, S. H. Wu, C. C. Wang, Y. F. Song, R. S. Liu, *J. Am. Chem. Soc.* **2016**, *138*, 8824–8833.
- [21] D. Goonetilleke, N. Sharma, W. K. Pang, V. K. Peterson, R. Petibon, J. Li, J. R. Dahn, *Chem. Mater.* **2018**, *31*, 376–386.
- [22] V. Baran, M. J. Mühlbauer, M. Schulz, J. Pfanzelt, A. Senyshyn, *J. Energy Storage* **2019**, *24*, 100772.
- [23] B. Dong, J. J. Biendicho, S. Hull, R. I. Smith, A. R. West, *J. Electrochem. Soc.* **2018**, *165*, A793–A801.
- [24] B. Vadlamani, K. An, M. Jagannathan, K. S. R. Chandran, *J. Electrochem. Soc.* **2014**, *161*, A1731–A1741.
- [25] M. Bianchini, J. B. Leriche, J. L. Laborier, L. Gendrin, E. Suard, L. Croguennec, C. Masquelier, *J. Electrochem. Soc.* **2013**, *160*, A2176–A2183.
- [26] B. Song, G. M. Veith, J. Park, M. Yoon, P. S. Whitfield, M. J. Kirkham, J. Liu, A. Huq, *Chem. Mater.* **2018**, *31*, 124–134.
- [27] F. Rosciano, M. Holzapfel, W. Scheifele, P. Novák, *J. Appl. Crystallogr.* **2008**, *41*, 690–694.
- [28] M. Heere, M. J. Mühlbauer, A. Schokel, M. Knapp, H. Ehrenberg, A. Senyshyn, *J. Appl. Crystallogr.* **2018**, *51*, 591–595.
- [29] R. Kataoka, T. Mukai, A. Yoshizawa, K. Inoue, T. Kiyobayashi, T. Sakai, *J. Electrochem. Soc.* **2015**, *162*, A553–A558.
- [30] A. J. Studer, M. E. Hagen, T. J. Noakes, *Phys. B: Condens. Matter* **2006**, *385–386*, 1013–1015.
- [31] T. C. Hansen, P. F. Henry, H. E. Fischer, J. Torregrossa, P. Convert, *Meas. Sci. Technol.* **2008**, *19*, 034001.
- [32] M. D. Frontzek, K. M. Andrews, A. B. Jones, B. C. Chakoumakos, J. A. Fernandez-Baca, *Phys. B: Condens. Matter* **2018**, *551*, 464–467.
- [33] A. A. Coelho, *J. Appl. Crystallogr.* **2018**, *51*, 210–218.
- [34] W. Branford, M. A. Green, D. A. Neumann, *Chem. Mater.* **2002**, *14*, 1649–1656.
- [35] M. R. Rowles, C. E. Buckley, *J. Appl. Crystallogr.* **2017**, *50*, 240–251.
- [36] NIST Center for Neutron Research "Neutron activation and scattering calculator" <https://www.ncnr.nist.gov/resources/activation/> Accessed 2022, May 18.
- [37] P. B. Samarasingha, J. Sottmann, S. Margadonna, H. Emerich, O. Nilsen, H. Fjellvåg, *Acta Mater.* **2016**, *116*, 290–297.

- [38] T. M. Sabine, B. A. Hunter, W. R. Sabine, C. J. Ball, *J. Appl. Crystallogr.* **1998**, *31*, 47–51.
- [39] G. Liang, V. K. Peterson, K. W. See, Z. Guo, W. K. Pang, *J. Mater. Chem. A* **2020**, *8*, 15373–15398.
- [40] J. H. Kim, C. S. Yoon, S. T. Myung, J. Prakash, Y. K. Sun, *Electrochem. Solid-State Lett.* **2004**, *7*, A216–A220.
- [41] C. K. Christensen, D. B. Ravnsbæk, *J. Phys. Energy* **2021**, *3*, 031002.

Manuscript received: July 16, 2022

Version of record online: September 15, 2022
